LEVEL

CURING STRESS FIELDS IN INVOLUTE EXIT CONES

Mechanics & Surface Interactions Branch
Nonmetallic Materials Division
Wright-Patterson Air Force Base, Ohio 45433

and

Prototype Development Associates, Inc.
Santa Ana, California 92705

DTIC
ELECTE
JUL 10 1980
S
C
D

ADA086404

DDC FILE COPY

80 7 7 066

NOTICE

When Government drawings, specifications, or other data are used for any purpose other than in connection with a definitely related Government procurement operation, the United States Government thereby incurs no responsibility nor any obligation whatsoever, and the fact that the Government may have formulated, furnished, or in any way supplied the said drawings, specifications, or other data, is not be be regarded by implication or otherwise as in any manner licensing the holder or any other person or corporations, or conveying any rights or permission to manufacture, use, or sell any patented invention that may in any way be related thereto.

This report has been reviewed by the Information Office (OI) and is releasable to the National Technical Information Service (NITS). At NTIS, it will be available to the general public, including foreign nations.

This technical report has been reviewed and is approved for publication.

N. J. PAGANO, Project Engineer
Mechanics & Surface Interactions Br.
Nonmetallic Materials Division

S. W. TSAI, Chief
Mechanics & Surface Interactions Br.
Nonmetallic Materials Division

FOR THE COMMANDER
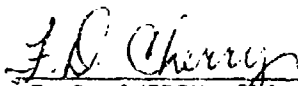
F. D. CHERRY, Chief
Nonmetallic Materials Division

AIR FORCE/56780/10 June 1980 — 370

REPORT DOCUMENTATION PAGE

READ INSTRUCTIONS
BEFORE COMPLETING FORM

1. REPORT NUMBER	2. GOVT ACCESSION NO.	3. RECIPIENT'S CATALOG NUMBER
AFML-TR-79-4191	AD-A086 404	

4. TITLE (and Subtitle)
CURING STRESS FIELDS IN INVOLUTE EXIT CONES

5. TYPE OF REPORT & PERIOD COVERED
Final Report
1 Nov 79 — 15 Feb 80

6. PERFORMING ORG. REPORT NUMBER

7. AUTHOR(s)
N. J. Pagano

8. CONTRACT OR GRANT NUMBER(s)

9. PERFORMING ORGANIZATION NAME AND ADDRESS
Materials Laboratory (AFWAL/MLBM)
Wright-Patterson Air Force Base, Ohio 45433 &
Prototype Development Associates, Inc.
Santa Ana, California 92705

10. PROGRAM ELEMENT, PROJECT, TASK AREA & WORK UNIT NUMBERS
24190310

11. CONTROLLING OFFICE NAME AND ADDRESS
Materials Laboratory
Air Force Systems Command
Wright-Patterson AFB, Ohio

12. REPORT DATE
February 1980

13. NUMBER OF PAGES
58

14. MONITORING AGENCY NAME & ADDRESS(if different from Controlling Office)
58

15. SECURITY CLASS. (of this report)
UNCLASSIFIED

15a. DECLASSIFICATION DOWNGRADING SCHEDULE

16. DISTRIBUTION STATEMENT (of this Report)
Approved for public release; distribution unlimited.

17. DISTRIBUTION STATEMENT (of the abstract entered in Block 20, if different from Report)

18. SUPPLEMENTARY NOTES

19. KEY WORDS (Continue on reverse side if necessary and identify by block number)

Involute exit cone
Rosette exit cone
Curing stresses
Process stresses

Ply pattern
PATCHES III
Finite element analysis

20. ABSTRACT (Continue on reverse side if necessary and identify by block number)
A procedure is developed for determining the unusual distribution of ply material in an involute exit cone and then it is used in an analysis of the curing stresses in an IUS exit cone billet. The ply pattern analysis produces three Euler angles at each material point that are used to define properties for a finite element model of the billet. Attention is focused on the delamination failure mode observed during post cure and large regions of cross-ply tension are shown to occur during cool down. Comparisons with autopsy data show that

(over)

DD $_{1 \text{ JAN } 73}^{\text{FORM}}$ **1473**   EDITION OF 1 NOV 65 IS OBSOLETE

the predicted ply fiber distribution is in good agreement with that observed in the IUS billet, while the finite element stress pattern seems to correlate with observed cracking patterns. Finally, a sensitivity study shows a striking dependence of the interlaminar normal stress on the orientation of the ply pattern on the cloth.

FOREWORD

AFML-TR-79-4191

TABLE OF CONTENTS

LIST OF ILLUSTRATIONS

LIST OF ..

SECTION I

INTRODUCTION

Involute construction[1] is an approach used in contemporary rocket nozzle technology for the fabrication of exit cones. The latter are bodies of revolution having the general appearance of a frustum of a cone; however, wall thickness and half-cone angle are usually variable quantities. The end planes are normal to the axis of revolution, and a short cylindrical region at the small end is used to attach the exit cone to the nozzle. Bodies formed using involute construction are made by laminating identical composite plies of uniform thickness (woven cloth reinforcement) in such a way that the trace of each interface in a plane normal to the axis of revolution terminates on the inner and outer surfaces of the body. This laminating procedure for a conical body, shown in Figure 1, causes each interface to extend to the extremities of the body in both the radial and axial directions.

In this report, we shall refrain from using the literal definition of the word "cone" given above except in the specific case when we refer to exit cones. We use the term "cross-section" to refer to a plane normal to the axis of revolution and "profile" to indicate the geometry in a meridional plane (θ = constant). Finally, the three-dimensional surface defined by the distorted ply within the structure, such as ABCD in Figure 1, will be called the "involute surface."

It has been shown (Reference 1) that, for a cylindrical involute, in which the body generated is a hollow circular cylinder, the involute surface is defined by

$$r \sin \alpha = \text{constant} \qquad (1)$$

where r is the usual radial coordinate in a cylindrical coordinate system and α represents the angle between the tangents to the circle and trace of the involute surface in the cross-section (a spiral) at a given point

---

[1] Involute construction formerly was known as rosette construction.
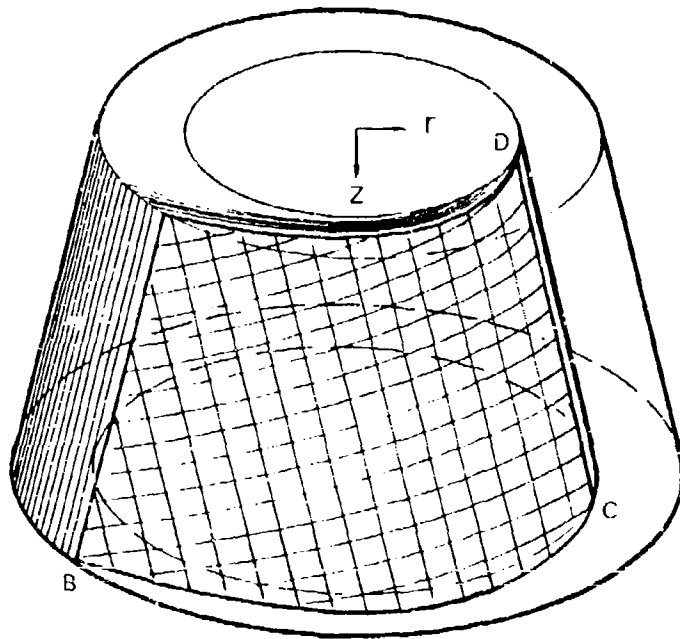
7-001029

Figure 1. Involute Exit Cone Ply Material Distribution

and is called the arc angle (Figure 2). To satisfy the requirement that consecutive plies form a continuous interface (no gaps or overlaps), the number of layers, N, is given by (Reference 1)

$$N = \frac{2\pi r \sin \alpha}{t_1} \qquad (2)$$

where t_1 is the ply thickness. The spiral equation is conveniently expressed in cylindrical coordinates by use of the relation

$$\theta - \theta_0 = \alpha + \cot \alpha - \alpha_0 - \cot \alpha_0 \qquad (3)$$

in junction with Equation 1, where (r_0, θ_0) are the coordinates of a given point on the curve and α_0 is the associated arc angle. Finally, the spiral length S between (r_0, θ_0) and (r, θ) is given by

$$S = \frac{r^2 - r_0^2}{2r \sin \alpha} \qquad (4)$$

The sign conventions associated with Equations 1 - 4 will be clarified in the next section.

Equations 1 - 4 provide an exact description of the geometry of involute cylinders. Flexible thin sheets stacked in accordance with these relations suffer no extensional or shearing strains. In the case of cones or more complex bodies, the surface of each composite sheet is doubly curved, hence exact development of the involute surface is not possible (Reference 2). In recognition of this fact, an approximate development procedure has been derived (Reference 3) to establish the flat sheet layout (called the ply pattern) corresponding to a given involute surface. This approach includes a method to predict the magnitude of the error involved in the approximation scheme. Although this approach yields an accurate ply pattern for practical involute bodies, it lacks convenience in characterizing the influence of differences in details of fabrication on the required geometric description of involute surfaces. Therefore, in the current work, we shall derive a new model that is sufficiently versatile to examine such effects.

3
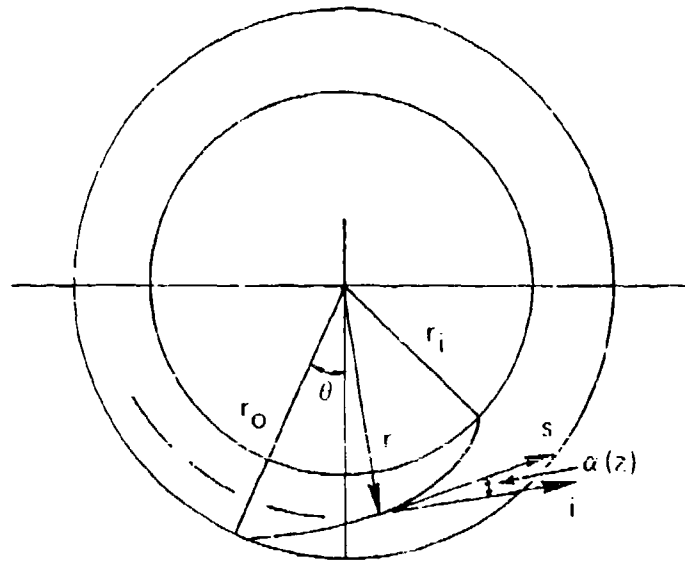
79001015

Figure 2. Involute Arc Angle

4

There is little work in the literature to describe the mechanical response of involute bodies. Only the stress field within an involute cylinder under various elementary loading conditions has been treated (Reference 1). It has been shown that an involute cylinder built from orthotropic sheets possesses, in general, 21 heterogeneous elastic constants in the cylindrical coordinate system. Despite this fact, axisymmetric response prevails under axisymmetric boundary conditions. The term axisymmetric as used here, however, only implies no theta dependence, as all stress and displacement components may differ from zero. In this work, we shall couple the involute geometric model with an existing variable property finite element program (PATCHES-III) to treat the mechanical response of general involute bodies under general axisymmetric boundary conditions with one element in the hoop direction. First, the quality of the present model will be examined by comparison with test data on an involute ring under post-cure conditions. Then, we shall apply this model to examine the nature of the stress and displacement fields developed during fabrication of an involute exit cone, their dependence on the material and geometric parameters of the structure, and their potential impact on process survival. Specific examples, involving the carbon-carbon billets used for the IUS[2] exit cones, will be solved and discussed relative to observed delamination failures following the post-cure phase of processing.

---

[2]Inertial upper stage. These bodies will be part of the space shuttle system.

SECTION II

SURFACE GEOMETRY

Consider an infinitesimal element of the involute surface in its cylindrical coordinate system as shown in Figure 3. Two sets of unit vectors are displayed in the figure: first, the right-hand system of basis vectors, $\vec{i}$, $\vec{j}$, $\vec{k}$, which are aligned in the positive θ, r, and z directions, respectively; secondly, the nonorthogonal system $\vec{t}$, $\vec{s}$, $\vec{n}$, where $\vec{t}$ is tangent to the meridian θ = constant, $\vec{s}$ is tangent to the trace of the involute surface in the cross-section z = constant, and $\vec{n}$ is the (outward) normal vector pointing away from the interior of the involute body. Also shown on Figure 3 are the arc angle α, the tilt angle γ, and the surface angle ψ, where

$$\vec{t} = \vec{j} \sin \gamma + \vec{k} \cos \gamma \tag{5}$$

$$\vec{s} = \vec{i} \cos \alpha - \vec{j} \sin \alpha \tag{6}$$

$$\cos \psi = \vec{t} \cdot \vec{s} \tag{7}$$

Substitution of Equations 5 and 6 into 7 reveals the interrelationship among the three angles

$$\cos \psi = -\sin \alpha \sin \gamma \tag{8}$$

We can remove ambiguity in signs by restricting the ranges of the angles according to

$$0 \leq \alpha \leq \pi/2, \ 0 \leq \gamma < \pi/2, \ \pi/2 \leq \psi < \pi \tag{9}$$

Also, the unit vector $\vec{n}$ can be found from the relation

$$\vec{n} \sin \psi = \vec{t} \times \vec{s} \tag{10}$$

All unit vectors and angles are shown in their positive directions in Figures 3 and 4.
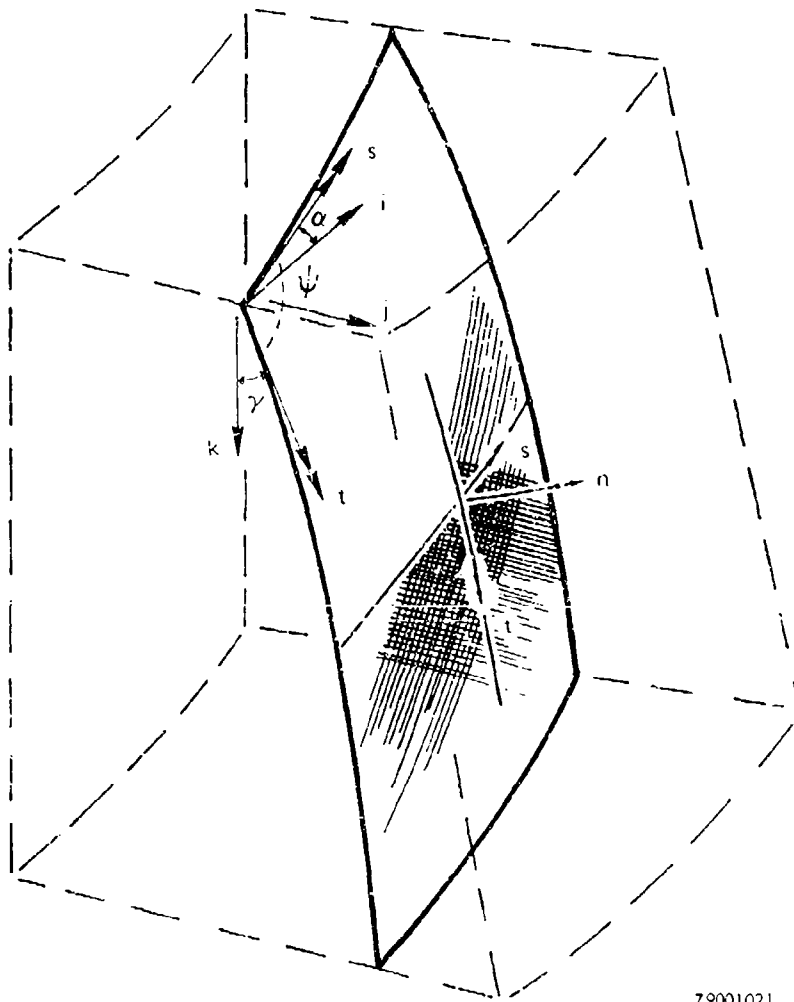
79001021

Figure 3. Unit Vectors for Cylindrical and Involute Coordinates

79001020
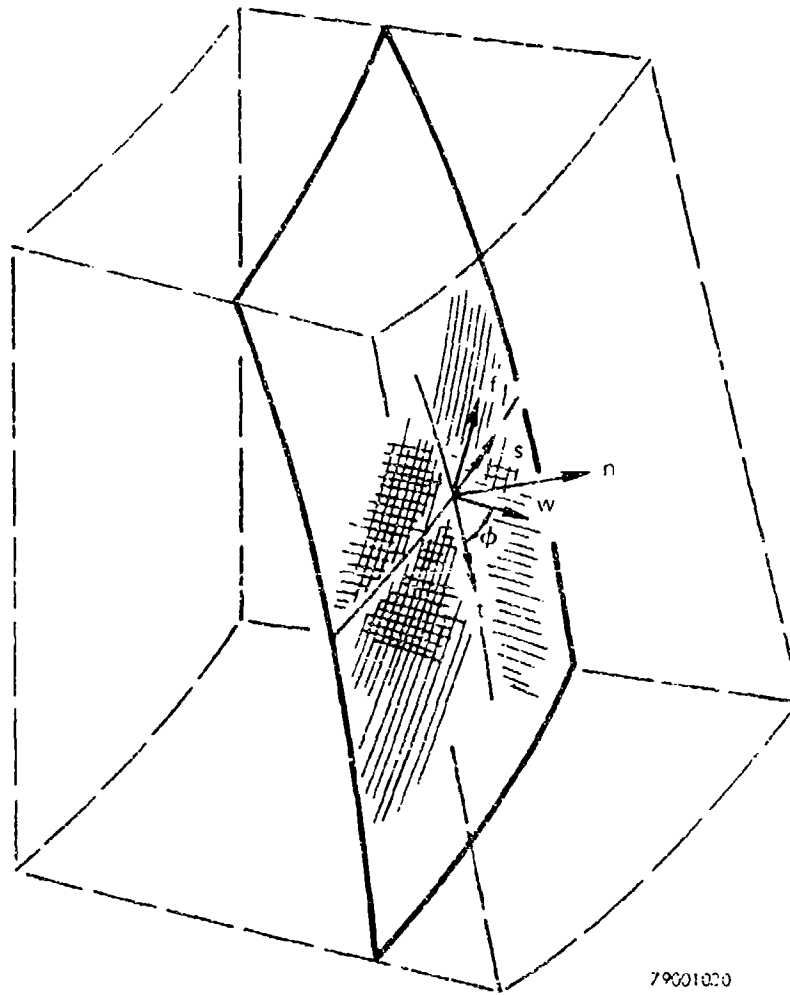
Figure 4. Unit Vectors for Ply Material Coordinates

The local elastic moduli depend upon the orientation of the two fiber directions within the cloth-reinforced composite. These are called the warp and fill directions, and are designated by unit vectors $\vec{w}$ and $\vec{f}$, respectively, as shown in Figure 4, where the helical angle ϕ between $\vec{t}$ and $\vec{w}$ is also displayed. At this point, we assume that the original right angle between the warp and fill directions is unchanged in the transformation from the ply pattern to the involute surface. Experimental measurements exist for two involute exit cones (References 4 and 5) which demonstrate the quality of this approximation. In both cases, only small distortions in the warp-fill angle occur except in transition regions where the cylindrical end intersects the main body of the exit cone. The present geometric and mechanical models lose accuracy in such regions proportional to any angular distortion present.

2.1 EULER ANGLES AND TRANSFORMATION LAWS

As discussed later, the use of conventional Euler angles represents a very convenient way to describe the influence of variable material orientation on anisotropic elastic moduli in conjunction with a variable property finite element analysis. Hence, at this point, we consider the definition of the Euler angles which transform unit vectors in the cylindrical coordinate system, $\vec{i}$, $\vec{j}$, $\vec{k}$, into the respective unit vectors in the planes of material symmetry, $\vec{w}$, $\vec{f}$, $\vec{n}$. The first transformation is a rotation about $\vec{k}$ through a Euler angle $-\alpha$. This carries $\vec{i}$ into $\vec{s}$, the unit vector along the horizontal spiral. Next, a rotation through an angle λ' about $\vec{s}$ takes place, where

$$\cos \lambda' = \vec{n} \cdot \vec{k} \tag{11}$$

Substituting Equation 10 into Equation 11 and making use of Equations 5, 6, and 8 leads to

$$\lambda' = -\cos^{-1} (\cot \alpha \cot \psi) \equiv -\lambda \tag{12}$$

where the negative sign is chosen to align the new orientation of $\vec{k}$ with $\vec{n}$. At this point, the vectors $\vec{w}$, $\vec{f}$ and the new position of $\vec{i}$ and $\vec{j}$ will

all be in the same plane. A final rotation of $\psi - \phi$ about $\vec{n}$ brings the two coordinate systems into coincidence. For notational convenience, we now let the coordinates corresponding to $(\vec{i}, \vec{j}, \vec{k})$ be represented by (x_1, x_2, x_3), respectively, and the analogous relation between $(\vec{w}, \vec{f}, \vec{n})$ and (x_1', x_2', x_3'), respectively. Letting $a_{ij} = \cos(x_i', x_j)$ these direction cosines are given by

$$a_{11} = \cos \alpha \cos (\psi-\phi) - \sin \alpha \cos \lambda \sin (\psi-\phi)$$

$$a_{21} = \cos \alpha \sin (\psi-\phi) + \sin \alpha \cos \lambda \cos (\psi-\phi)$$

$$a_{31} = \sin \alpha \sin \lambda$$

$$a_{12} = - \sin \alpha \cos (\psi-\phi) - \cos \alpha \cos \lambda \sin (\psi-\phi)$$

$$a_{22} = - \sin \alpha \sin (\psi-\phi) + \cos \alpha \cos \lambda \cos (\psi-\phi)$$

$$a_{32} = \cos \alpha \sin \lambda$$

$$a_{13} = \sin \lambda \sin (\psi-\phi)$$

$$a_{23} = - \sin \lambda \cos (\psi-\phi)$$

$$a_{33} = \cos \lambda \tag{13}$$

Finally, letting $C_{ijk\ell}$ and $C_{ijk\ell}'$ denote the effective stiffness coefficients in x_i and x_i' coordinates, respectively, they transform according to

$$C_{ijk\ell} = a_{mi} \, a_{nj} \, a_{pk} \, a_{q\ell} \, C_{mnpq}' \tag{14}$$

The material is assumed to possess local orthotropic symmetry, hence only nine independent stiffness coefficients exist in the primed coordinate system.

The equations developed in this section are quite general in nature. With the exception of Equations 1 - 4, the expressions are valid for arbitrary surfaces of an elastic body in which the axes of material symmetry remain orthogonal. In the next section, the specific case of an involute body shall be treated, and a model to identify the appropriate geometric parameters for this special class of problems will be given.

2.2 INVOLUTE SURFACE MODEL

Aside from the case of involute cylinders, the fundamental equations that describe the geometry of involute bodies are not exact. As mentioned earlier, an involute body is formed (at least in theory) by laminating identical plies of uniform thickness in such a way that each ply extends to the extremities of the body in both the r and z directions with perfect continuity. A rigorously valid solution for a surface satisfying these requirements has not been established. In fact, the very existence of such a solution has not been demonstrated.[3] An approximate solution for a conical body has recently been presented by Pagano and Hsu (Reference 3), where the impossibility of developing the involute surface from a flat sheet was also shown. Fortunately, in practice, arc angles are generally quite small, usually less than seven degrees, so that the effects of geometric errors in ply pattern analysis do not appear to be critical except in the aforementioned juncture regions. In this section, we shall present an approximate representation of the involute surface leading to a new model for the ply pattern geometry which is more versatile and compatible with existing finite element computer codes than that given in Reference 3. The capability of this model to use the ply pattern and appropriate geometric data to define the associated involute surface will be shown and demonstrated for an IUS exit cone.

As in Reference 3, we begin by assuming the trace of the involute surface in a plane z = constant is given by

$$r \sin \alpha = C(z) \tag{15}$$

where C is a function of z alone. This is a logical extension of Equation 1, which satisfies the involute requirements in a plane. Furthermore, we shall restrict our attention to the limiting case of small α ($\alpha \ll 1$) from the outset. In this case, Equation 15 becomes

$$r\alpha = C(z) \tag{16}$$

---

[3]Analyses which attempt to either confirm or deny the existence of such a solution are presently being conducted by the author. An updated version of this work will be reported shortly.

We again follow Reference 3 by approximating the relationship between t', the actual layer thickness, and t_1, the layer thickness measured in the cross-section by

$$t' = t_1 \cos \beta \tag{17}$$

where β is chosen as the local half-angle defined by the centerline of the profile. In general, β depends upon z. Thus the parameter $C(z)$ is given by

$$C(z) = \frac{Nt'}{2 \pi \cos \beta} \tag{18}$$

which follows from Equations 17 and 2. The geometry of the involute surface is thus defined by a spiral trajectory in each cross-section of the form given by Equation 3. Hence, if we consider two points lying on a trace of the involute surface in a cross-section, e.g., (r_1, θ_1, z) and (r_2, θ_2, z), the small α approximation yields

$$\theta_2 - \theta_1 = \frac{1}{\alpha_2} - \frac{1}{\alpha_1} \tag{19}$$

In conjunction with Equation 16, this establishes the direct relation in cylindrical coordinates

$$r_2 - r_1 = C(\theta_2 - \theta_1) \tag{20}$$

Letting arc length be denoted by S, Equations 4 and 15 give

$$S_2 - S_1 = \frac{1}{2C} (r_2^2 - r_1^2) \tag{21}$$

In practical applications, the body profile is expressed in digital form, rather than in a continuous manner. Hence, functional variations along the meridians are expressed in piecewise continuous fashion. For improved accuracy, a finite difference representation using small elements is employed. Considering two points on a meridian, (r_1, θ, z_1) and (r_2, θ, z_2), $z_2 > z_1$, we use the approximation

$$\tan \gamma_1 = \tan \gamma (r_1, z_1) = \frac{r_2 - r_1}{z_2 - z_1} \tag{22}$$

12

while Equations 8 and 22 give

$$\cos \psi_1 = \frac{c(r_1 - r_2)}{ar_1} \qquad (23)$$

approximately, where

$$a^2 = (r_2 - r_1)^2 + (z_2 - z_1)^2 \qquad (24)$$

If given the number of layers N, the layer thickness t', and the body profile, Equations 18 and 20 are sufficient to define the entire involute surface. Equations 19 and 21 - 23 give other geometric relations required in the subsequent approximate development of the surface, as well as those needed to define the first two Euler angles. The definition of the third Euler angle follows from the ply pattern analysis treated in the next section.

2.3 PLY PATTERN ANALYSIS

In our approximate development procedure, each point in the developed figure (ply pattern) is mapped into its image on the involute surface. In this scheme, we assume that the local arc length ΔS and local angle ψ between the meridian and spiral tangent are preserved in the mapping process. It will also be necessary to prescribe the transformed position of a given line in the ply pattern. The recursion scheme employed is shown in Figure 5, where $\Delta S_1^{(i)}$ and $\psi_1^{(i)}$ are defined by their counterparts on the involute surface. The procedure involves marching along two lines of constant z, which represent their respective spiral trajectories in the involute surface. For convenience, a constant step size of $\Delta \theta = \theta_2 - \theta_1$ is utilized. The upper line (subscript 1) is defined by the true arc distances (as represented by short chords) along this line. The lower line (subscript 2) is only tentatively established. This is due to the fact that we have represented the functions β_2 and ψ_2 by backward differences. By comparison of the trajectories in the ply pattern at a given value of z, first at the lower level and then at the upper level in the next cycle, we can control errors created by this source.
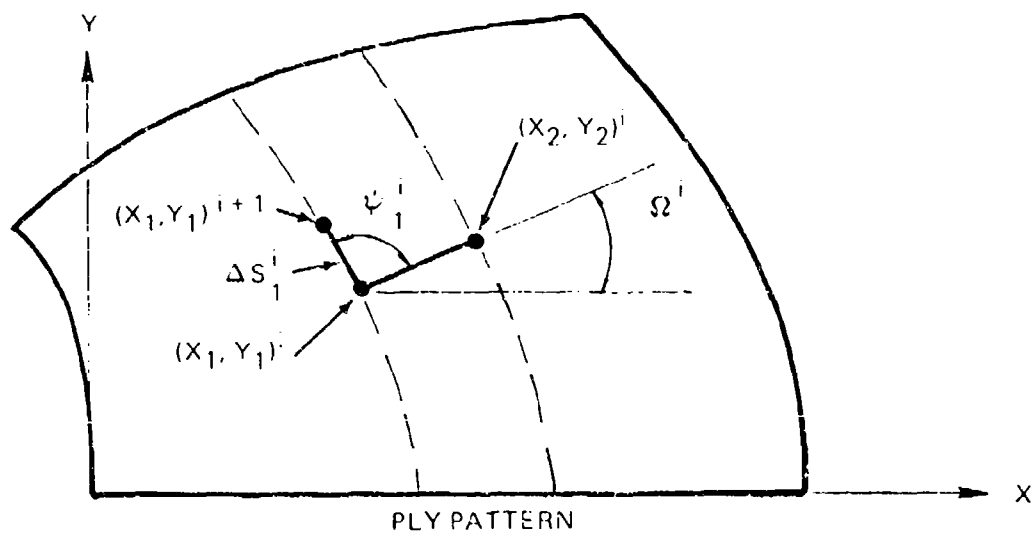
PLY PATTERN

79001027

Figure 5. Ply Pattern Analysis for an Involute Line

The shallow gradients of β and ψ in the z direction in practical exit cones also tend to minimize these errors. Letting X and Y be orthogonal coordinates in the plane of the ply pattern, the recursion formulas are given by

$$X_j^{(i+1)} = X_j^{(i)} + \Delta S_j^{(i)} \cos (\psi_j^{(i)} + \Omega^{(i)}) \quad , \quad j = 1,2$$

$$Y_j^{(i+1)} = Y_j^{(i)} \quad \Delta S_j^{(i)} \sin (\psi_j^{(i)} + \Omega^{(i)}) \quad , \quad j = 1,2 \tag{25}$$

where

$$\tan \Omega^{(i)} = \frac{Y_2^{(i)} - Y_1^{(i)}}{X_2^{(i)} - X_1^{(i)}} \tag{26}$$

It is understood that the functions corresponding to subscript j = 2 in Equations 25 and 26 are only approximate (beyond the other approximations we have employed). They are, however, used to represent the equation of the lowest edge of the ply pattern. If the correspondence between a line in the ply pattern and its image on the involute surface is established, e.g., the transformed position of the left-hand edge of the ply pattern, only N and t' are needed to complete the approximate development procedure. Since this correspondence is not generally known, iterative techniques become necessary. Before we proceed to discuss a practical application of this work, we should observe that the helical angle ϕ can be expressed as

$$\phi = \phi_0 - \Omega \tag{27}$$

as shown in Figure 6, where ϕ_0 is the angle between the warp direction in the ply pattern and the X-axis, while Ω, the angle indicating the orientation of the meridian in the ply pattern at the point of interest, is given by Equation 26.
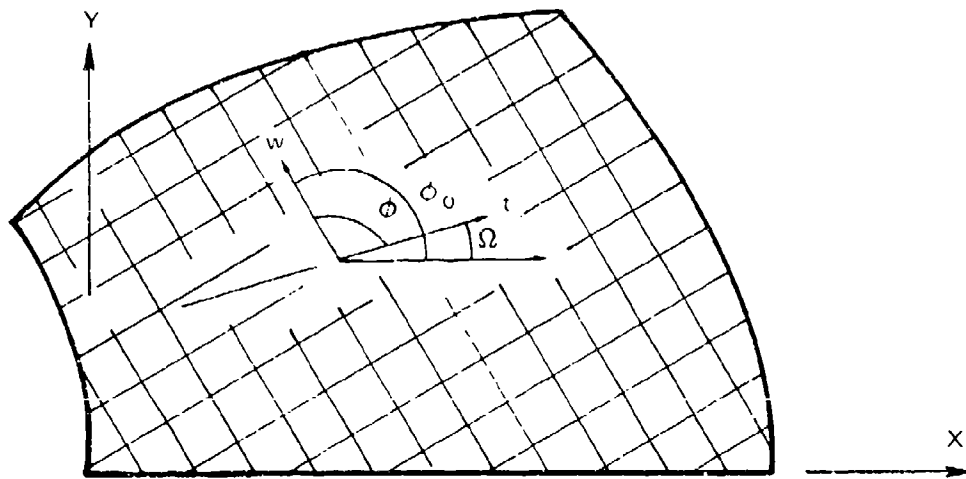
79001028

Figure 6.   Ply Pattern Helix Angle

16

2.4 INVERSE PROBLEM SOLUTION

The specific problem under consideration involves the inverse of that
which we have just described. In this case, the ply pattern is given,
and the involute surface is sought. Although the basic equations are
the same, analysis details differ in this case. In order to clarify the
nature of this problem, we shall present a brief outline of the fabri-
cation approach used in the manufacture of the IUS exit cones.

In its initial form, the preimpregnated cloth material used in the
construction is uncured and very thick (approximately twice the final
cured thickness). It is in this form that the material is cut into the
ply pattern. Once the plies are cut, they are laminated, with the inner
surface being controlled by a conical male mandrel. In this initial
state, the left-hand edge of the ply pattern lies along the generator of
the mandrel. Because of the large thickness in this form, the involute
surface differs considerably from that in the final state. The material
is then placed in a female mold die and debulked and cured under
temperature and pressure. The ply thickness is greatly reduced in this
phase. Finally, the cured billet is removed from the mold die and
post-cured. Thus, the final _outer_ surface of the body is controlled
while the location of the initial straight edge of the plies is not
known in the final configuration. The situation is aggravated by the
machining which takes place on the inner surface following the cure
process. Although the amount of material removed in machining is not
great, it is sufficient to preclude direct comparison of the model
prediction against the dimensions of the actual structure.

The following approach was devised to define the involute surface
and its associated orientation vectors corresponding to the given ply
pattern. First, an assumption is invoked to establish the transformed
position of the left-hand edge of the ply pattern. The assumption made
is that this line lies on a meridian in the structure. Note that this
does _not_ imply that the straight edge of the ply pattern follows a
generator of a cone. Furthermore, the edge will not, in general, remain
straight within the structure. We then start at the inner (machined)

radius and march along the mapped spiral trajectory until this curve intersects the right-hand boundary of the ply pattern. This leads to a computed radius, say $\bar{r}_1$, which differs from that prescribed at this level, say r_1. The inner radius is then corrected by use of the relation

$$S_1 = \frac{\bar{r}_1^2 - \overset{(1)}{r_1^2}}{2c} = \frac{r_1^2 - \overset{(1)}{\bar{r}_1^2}}{2c} \tag{28}$$

or

$$\overset{(1)}{\bar{r}_1^2} = r_1^2 - \bar{r}_1^2 + \overset{(1)}{r_1^2} \tag{29}$$

where $\overset{(1)}{r_1}$ is the assumed (machined) inner radius and $\overset{(1)}{\bar{r}_1}$ the corrected inner radius. This approach employs the arc length on the ply pattern and outer radius as control parameters, which is consistent with the manner in which the involute body has been formed. To define the required intersection, the right-hand boundary of the ply pattern has been modeled as a series of parametric cubic lines for the local X, Y coordinates.

The above analysis may be viewed as the first cycle of an iteration scheme to define the involute geometric parameters. Subsequent iterations can be accomplished in the same fashion after accounting for the corrected θ variation on the inner surface. Only one iterative cycle has been used in the present work, since this was sufficient to guarantee negligible change in the Euler angle distribution as computed from the assumed and corrected radii. Also a reasonable correspondence between calculated and measured (machined) inner radii has been achieved. This correspondence is shown in Table 1 for typical IUS ply patterns.

TABLE 1

SRM-2 EXIT CONE INNER RADII COMPARISONS

Axial Station	R Machined	R_C Computed*	R_A Computed*
4.00	4.05	3.80	---
6.00	5.00	4.99	---
8.00	5.93	5.67	---
10.00	6.80	6.60	---
10.95	7.21	7.08	---
14.00	8.48	8.39	8.44
16.00	9.25	9.24	9.28
18.00	10.04	10.05	10.07
20.00	10.78	10.76	10.76
22.00	11.48	11.45	11.43
24.00	12.15	12.10	12.08
26.00	12.80	12.74	12.71
28.00	13.45	13.39	13.34
30.00	14.04	13.98	13.96
32.00	14.60	14.55	---
34.00	15.15	15.11	---
35.25	15.50	15.45	---

*Computed from ply patterns C and A.

SECTION III

3D INVOLUTE FINITE ELEMENT MODEL

Axisymmetric bodies of involute composite construction also present difficult finite element modeling problems because of their unusual property distributions. The constantly changing orientation of the warp and fill directions in a billet (Figure 4) cause all 21 elastic constants and all six coefficients of thermal expansion to vary as functions of radius and axial station (Equation 14). To model this unusual material the variable property 3D finite element (Reference 6) in PATCHES-III (Reference 7) was used with generalized axisymmetric constraints. (Computationally more efficient 2D finite elements for axisymmetric problems with torsion have subsequently been added to PATCHES-III.) The material representation problem is solved with these finite elements by allowing all material properties to be independent functions of position in the element. A key ingredient to the practical as well as mathematical success of this approach is the use of Euler angles[4] to implicitly define the property distribution functions. This reduces the input material data requirements from 27 nonlinear functions to three quasilinear functions, plus the ply orthotropic ply material constants. A brief mathematical description of the property model and the finite element model are presented next.

3.1 PROPERTY DISTRIBUTION MODELING

The stress-strain transformation at a material point in orthogonal coordinates may be expressed using contracted notation as

$$\sigma_i = C_{ij}[\epsilon_j - \alpha_j \Delta T] \text{ for } 1 \leq i, j \leq 6 \qquad (30)$$

where, for an involute body in cylindrical coordinates,

$$C_{ij} = C_{ij}(r, z)$$
$$\alpha_i = \alpha_i(r, z) \qquad (31)$$

---

[4]Three body-fixed rotations (A, B, C) define the Euler angles used in PATCHES-III.

indicates the spatial material variability. Note that in both cylindrical and Cartesian coordinates, all components in Equation 31 are nonzero functions of r and z for an involute cone. These functions can be defined using Euler angles and the ply material properties as follows

$$C_{ij}(r, z) = C'_{k\ell} \, D_{ki}(r, z) \, D_{\ell j}(r, z)$$

$$\alpha_j(r, z) = \alpha'_m \, D^{-1}_{jm} \tag{32}$$

where Equations 13, 14, 25, 26, and 27 induce

$$D_{ki}(r, z) = D^*_{ki}(A(r, z), B(r, z), C(r, z)) \tag{33}$$

and typical finite element input data are

$$A(r, z) = A(r(\xi_k), z(\xi_k))$$

$$= A^*(\xi_k) \tag{34}$$

The $C'_{k\ell}$ are the _in situ_ stiffness coefficients of a ply in $\vec{w}, \vec{f}, \vec{n}$ coordinates. These properties are constant over the entire dimension of every ply in an ideal involute body. The notation D^*_{ki} indicates the function induced by reparameterization of the function D_{ki} and this same notation is applied for any function induced by reparameterization. The functions $A^*(\xi_k)$, $B^*(\xi_k)$, and $C^*(\xi_k)$ can be up to tricubic Hermitian, but trilinear functions are adequate for involute bodies.

The D_{ki} matrix is, of course, the strain transformation in contracted notation and consists of the product of direction cosines. Equations 13 define the direction cosine matrix in terms of the Euler angles computed from the ply pattern analysis and these angles are directly input to PATCHES-II!

$$A = -\alpha$$

$$B = \lambda$$

$$C = \psi - \phi \tag{35}$$

Note that these rotations take the $\vec{i}$ axis onto a warp fiber, and the $\vec{k}$ axis becomes a normal vector to the tangent plane of the ply at each material point. Note also that for Cartesian finite element models, the first rotation must be increased by the local cylindrical coordinate, $A = -\alpha -\theta$. The exact relation between the D_{ki} and the a_{mn} depends on the specific contracted notation convention used by the finite element program. The convention used in PATCHES-III and in Reference 1 are different.

The spatial distribution functions for an involute composite can now be defined for the finite element model in very simple terms. Values of the three Euler angles at the corners of an element completely define the spatial orientation of all ply material within any element. In PATCHES-III the variable Euler angle data are defined for each finite element using the same interpolation functions that define the shape of the element (Reference 6). The data functions are constructed by the program, usually from corner grid point values. Since the ply material properties are constant, the orientation functions completely define the involute property distribution functions for a finite element. This is illustrated in Figure 7, which shows the three Euler angles as a function of radius for a cone geometrically similar to the IUS exit cone. Note the large variation in the last rotation angle. This is a measure of the change in the angle between the hoop direction and the local warp direction through the thickness of the cone. These angles are computed in the local tangent plane of a ply using the ply pattern analysis developed earlier. What this large change indicates physically is that the high modulus fibers vary from a meridional direction on the inside to predominately a hoop direction on the outside. This behavior is typical of thick-walled involute cones.

3.2 FINITE ELEMENT MATRIX MODEL

A definition of the 3D finite element model is provided to indicate the major steps in the generation of a stiffness matrix for
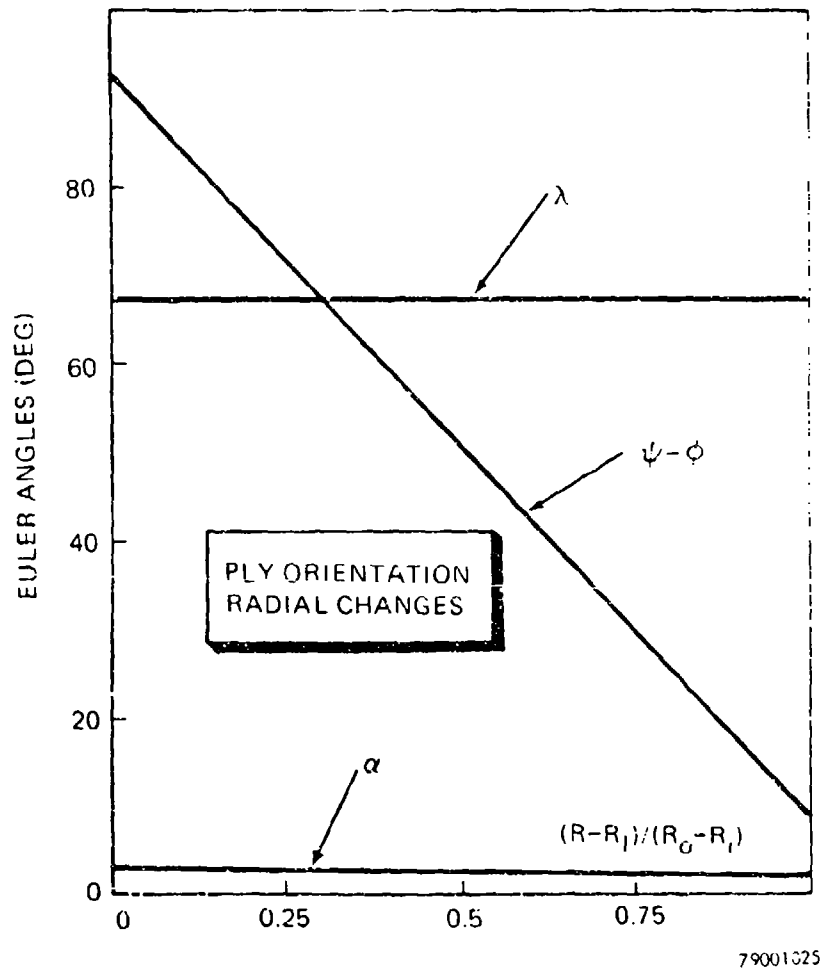
Figure 7. Euler Angle Radial Variation

an involute composite. Given the shape of an element in parametric coordinates $z_i(\xi_k)$, the stiffness matrix can be written

$$[K] = \int_0^1 \int_0^1 \int_0^1 [P]^T[B]^T[D]^T[C'][D][B][P] \det J \, d\xi_1 d\xi_2 d\xi_3 \qquad (36)$$

where

$[C'] = C'_{k\ell}$ Ply Stiffness Coefficients

$[D] = D^*_{ki}(A^*, B^*, C^*(\xi_m))$ Involute Strain Transformation

$[B] = B_{im}(z_i(\xi_j))$ Strain-Displacement Equations

$[P] = P_{mn}(\xi_j)$ Tricubic Hermite Displacement Functions

$J = z_i, _{\xi_j}$ Jacobian of the Shape Function

The integrations result in a 64 node 3D finite element that must be constrained to 16 independent nodes for axisymmetric problems. If cylindrical rather than Cartesian strain-displacement equations were used to form [B], one integral is simply $\Delta\theta$ and the generation becomes much simpler.

The general axisymmetric problem has a torsional displacement component and this twisting response is very important to the interlaminar stress response of an involute composite. To use a 3D Cartesian finite element for this class of problems the analysis coordinate frame at each node must be converted to cylindrical and then equality constraints applied in the hoop direction.

$$[K_{AXY}] = [T_X]^T[T_R]^T[K][T_R][T_X] \qquad (37)$$

where

$[T_R]$ = Cylindrical Coordinate Transformation

$[T_X]$ = Nodal Equality Constraints

24

and the nodal equality constraints are of the form

$$U_{ijk} = \delta_{i\ell} \, \delta_{jm} \, T_{kl} \, U_{\ell ml} \quad \text{for} \quad 1 \leq i, j, k \leq 4 \tag{38}$$

The 64 nodes of the 3D element result from four nodes in each parametric direction. The 16-node axisymmetric element results from equality constraints in the third parametric direction

$$T_{1k} = (1, 1, 1) \tag{39}$$

where the shape function for the finite element $z_1 (\xi_k)$ is constructed to have ξ_3 coincide with the hoop direction. The computational details of how to efficiently perform the generation and constraint operations will not be presented in this report.

3.3 MODEL VERIFICATION

The first analysis of an involute body to include all material coupling terms was that of Reference 1 for a cylinder. The finite difference model used in that analysis has subsequently been experimentally verified in the linear elastic range (Reference 8). The present finite element model was first checked against that finite difference solution by using a single 3D element. All stress and strain results compared within five percent for the pressure load problem analyzed in Reference 1. To verify the model in a thermal load case, experimental data from an Aerojet Solid Propulsion Company involute test cylinder were used. The test data consists of diametral expansion measurements during post-cure heating of the cylinder. Note that both thermomechanical and thermochemical phenomena contribute to the dimensional changes at the higher temperatures. All these effects were lumped together and represented using temperature-dependent thermal expansion properties for the ply material. At the lower temperatures, excellent agreement was obtained, as Figure 8 shows, and good agreement was obtained over the entire post-cure range. These results indicate that the present finite element, with variable property modeling, can be used to represent both the thermal and mechanical response of bodies of involute construction.

25
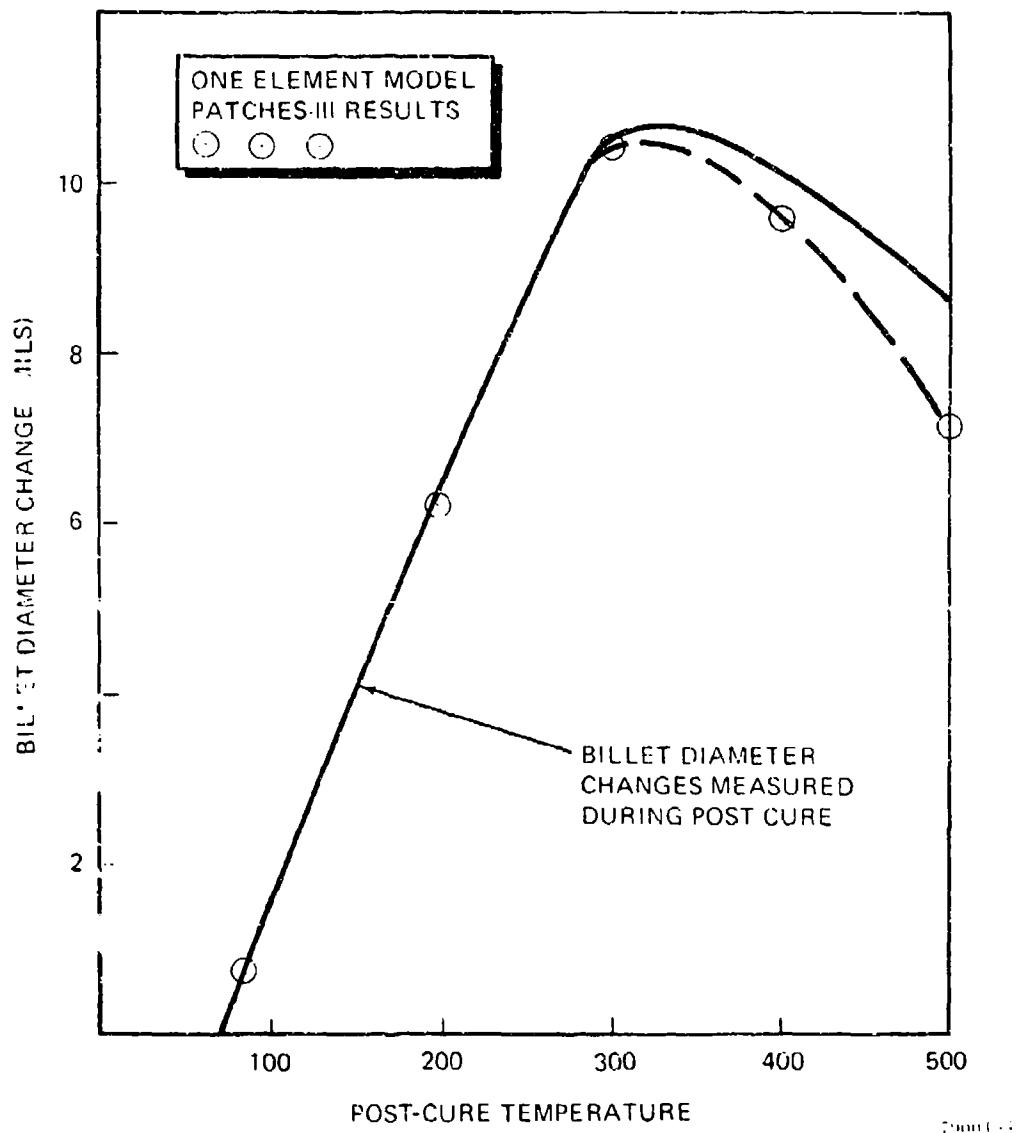
Figure 8. Post-Cure Diametral Expansion Comparisons

SECTION IV

IUS EXIT CONE BILLET MODELING

The involute construction described earlier produces a billet of graphite-phenolic material that after post cure is subsequently carbonized and graphitized to form a carbon-carbon billet. Post cure is the critical processing step for most billets; and, delamination is the failure mode typical of thick-walled billets. In this section we will examine a specific billet from the IUS project for the SRM-2 motor. This particular billet delaminated sometime during post cure and an autopsy was performed that allows several aspects of the present involute modeling to be evaluated. Comparisons are made with the as-built geometry and Euler angle distributions that show remarkably good agreement over most of the billet. They also show a region in the neck area where rapid changes in curvature cause ply distortion and other local differences in the property distribution between the ideal ply model and the actual billet.

The ply pattern used to form the SRM-2 billet is shown in Figure 9, with the z cross-section involute traces also shown as they were computed by using the present analysis (Equations 25 and 26). The warp and fill directions are aligned with the X, Y axes as the ply is cut from the graphite cloth. In a later section, other orientations of the pattern on the cloth will be examined for process stress sensitivity. The ply involute surface is shown in Figure 10 constructed from involute arcs blended together to form a surface[5] with continuous tangent vectors as the ply would appear in the billet after the cure cycle; and, there are 176 identical plies in one billet. Note the unusual surface grain (Figure 11) associated with the outer edge of each ply. The actual billet shows this same surface grain with noticeable differences only in the neck region. The weight of the ply analysis model and the actual billet are compared in Table 2. Note that the in situ ply surface area was used to compute the model weight by assuming a uniform thickness

---

[5]The involute surface figures were not computed as part of the ply pattern analysis.
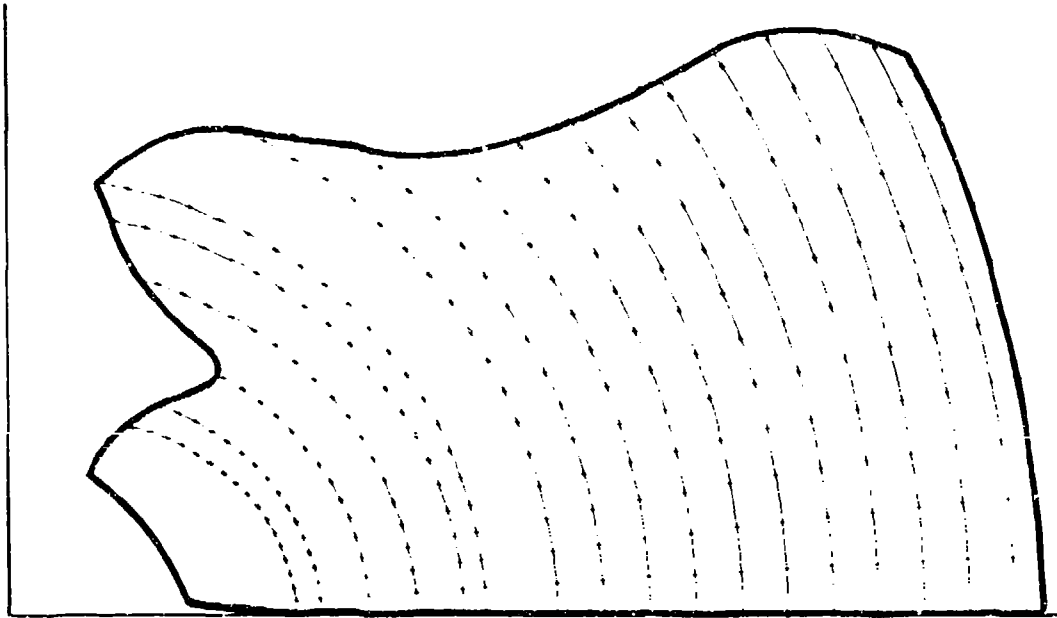
79001.033

Figure 9.   Ply Pattern A Analysis Results
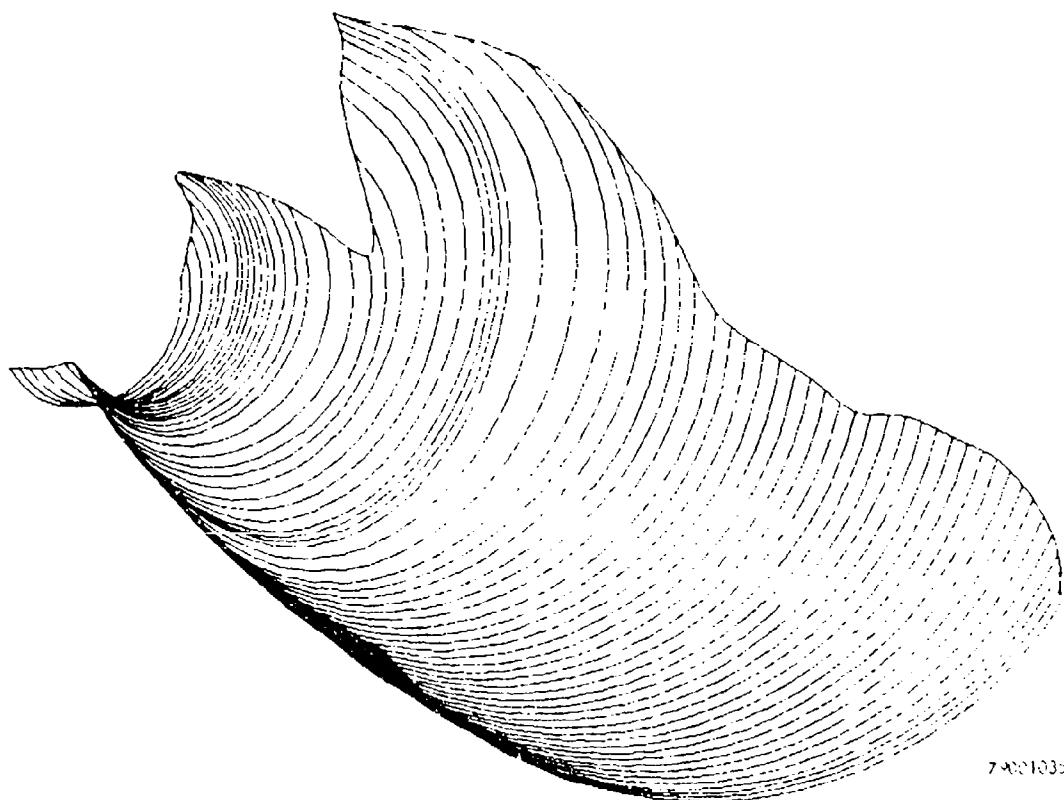
Figure 10.   Ply Pattern A Involute Surface
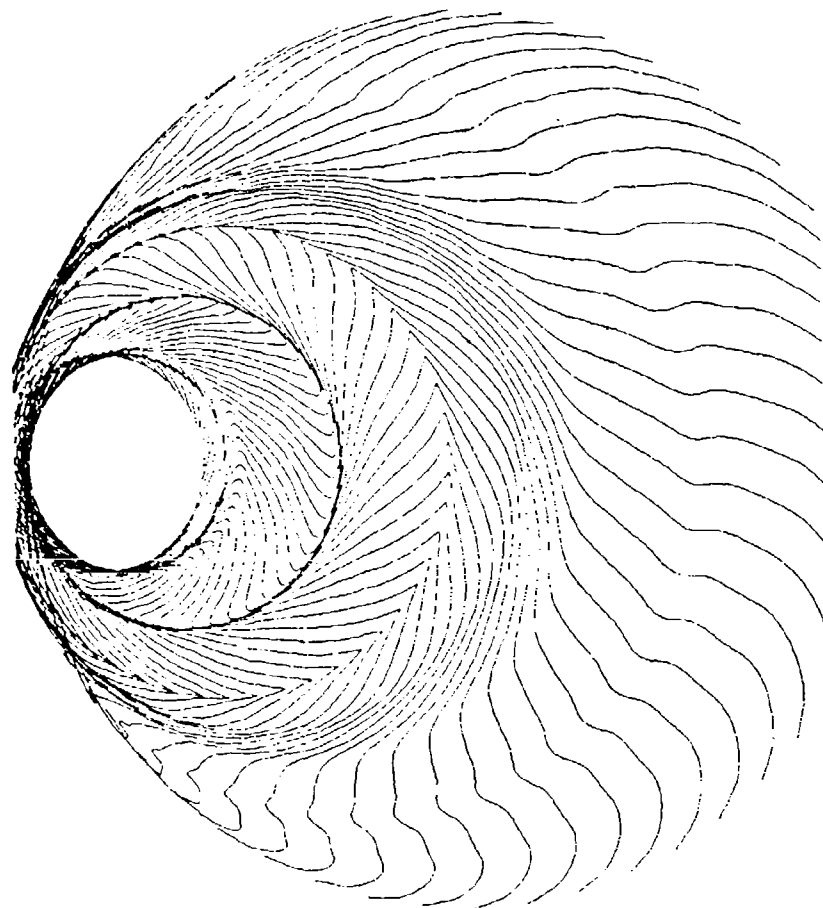
7 2061034

Figure 11. Billet Exterior Surface for Ply Pattern A

TABLE 2

BILLET AND MODEL DATA COMPARISONS

Data	Ply Model	Finite Element Model	Billet
Volume	1962 in.^{3}(32155 cm^3)	2909 in.^{4}(34249 cm^3)	----
Weight	101* lbs (449N)	107* lbs (476N)	108 lbs (480N)

*At sea level for 1.42 g/cc weight density.

(0.0123 inch) and density, and sea-level gravity. The weight of the finite element model is also included in Table 2 based on the same weight density, but a completely different geometry model.

The orientation of the warp and fill fibers were measured as a function of radius at several axial stations by Buch and Pfeifer in their autopsy on the IUS billet at the Aerospace Corporation. A typical variation is shown in Figure 12 for a specimen taken from the small diameter end of the billet and fingerprinted. Their data correspond to the angle ϕ in third Euler angle, $\psi - \phi$, where the angle ψ changes very little with r for small arc angles (Equation 8). A comparison of their data and the ply pattern analysis results for $\phi(r)$ at the maximum thickness station shows excellent agreement (Figure 13). Note also the near perfect linearity of the data over a very large change in warp orientation.

Consider next a profile section of the billet subdivided into eighteen 3D finite elements (Figure 14). The maximum thickness station, 10.95, is well away from the cone-cylinder transition where ply distortions occur during fabrication. A comparison of the net warp rotation at various axial positions (Figure 15) shows the present model over-predicts this change in the neck area, but is otherwise in good agreement with the autopsy data. The neck area is a region of rapid change in half-cone angle that requires the ply to be distorted (i.e., strained) even before it is debulked. Measurements of this distortion (Reference 5) on plies

WARP/FILL
ORIENTATION
THROUGH THE
THICKNESS AFTER
POST CURE
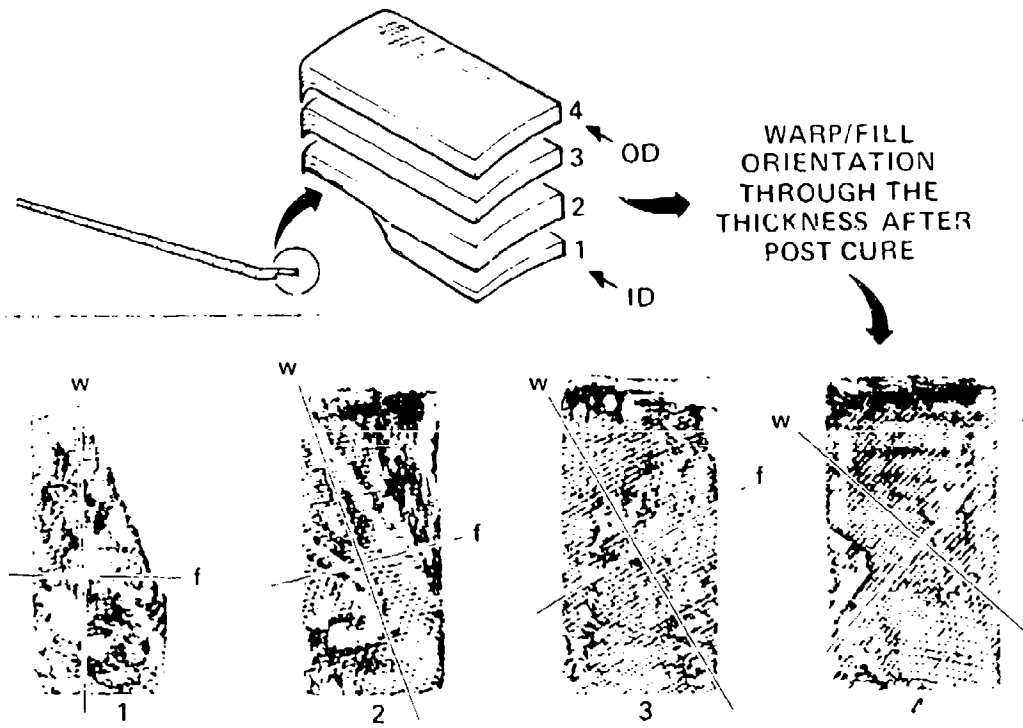
Figure 12.   Warp/Fill Fingerprints Through the Thickness
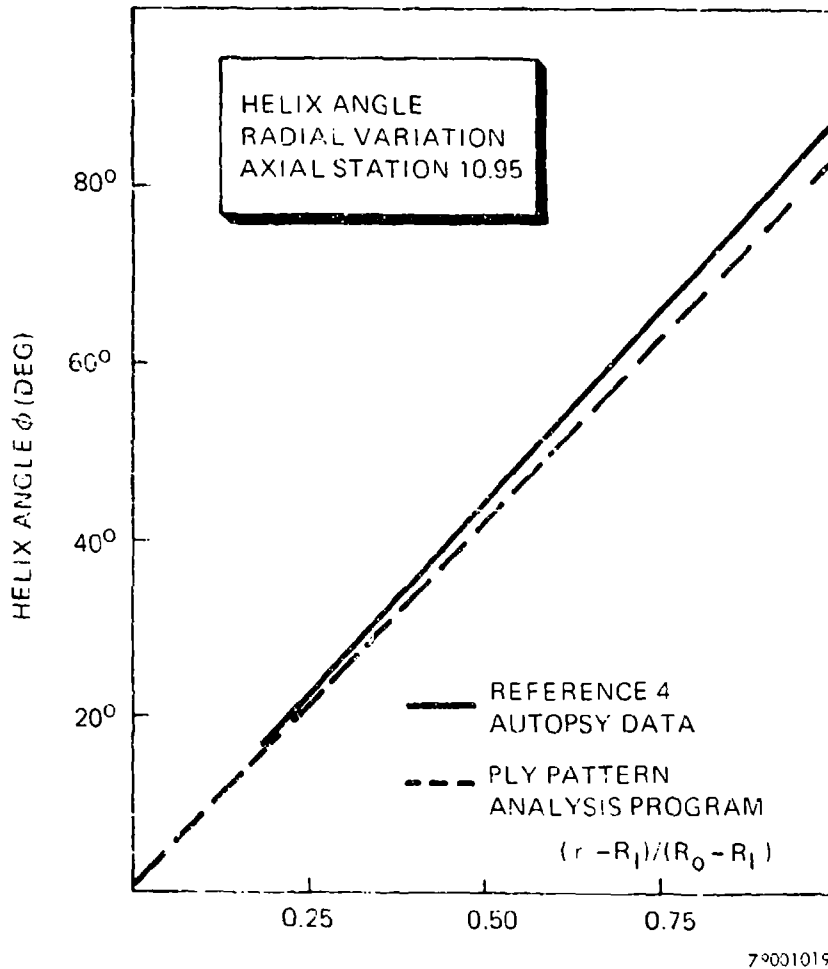
Figure 13. Helix Angle Radial Variation

ELEMENT SIX

113

111

6

13

11

SRM−2 BILLET
PATCHES−III MODEL
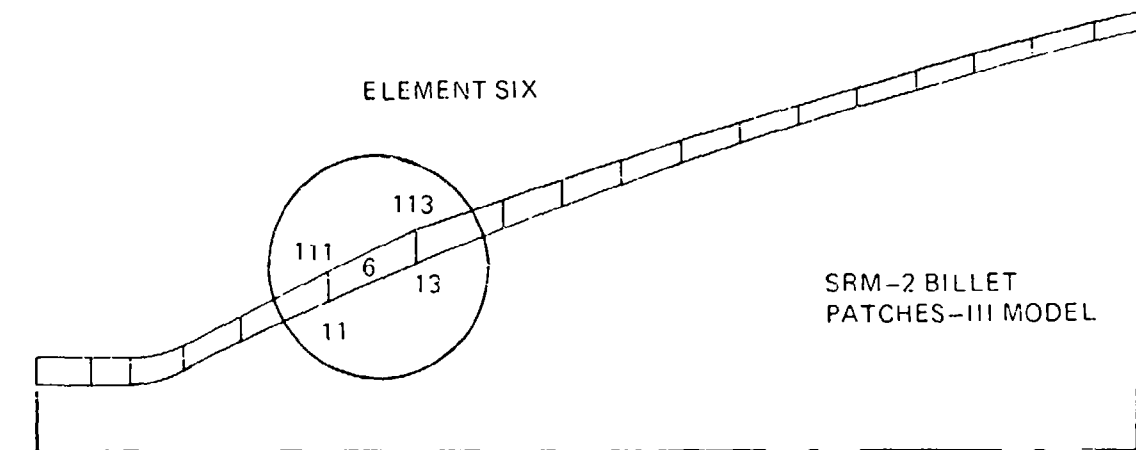
79001016

Figure 14.   PATCHES-III Finite Element Model of Billet
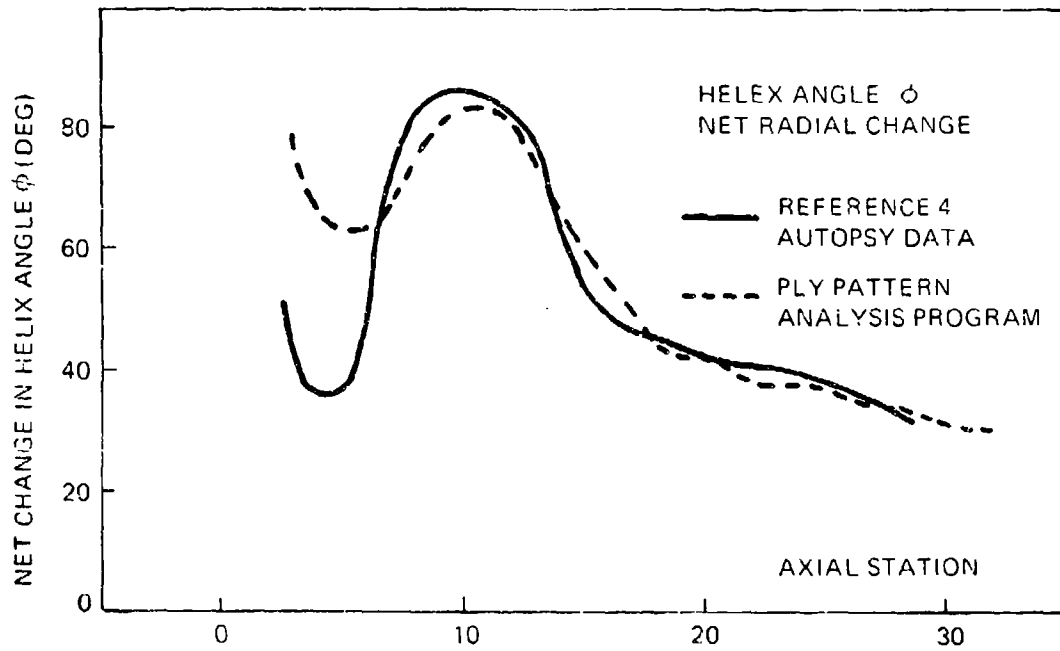
Figure 15. Helix Angle Changes Versus Axial Station

of similar size and material show up to a 10° loss in orthogonality between warp and fill. Other distortions occur during debulking that cause $\phi(r)$ to be locally nonlinear, a condition that acts to reduce the net warp rotation in the neck.

After the warp-fill orientation functions are known, the stiffness properties of the exit cone billet are computed by using Equation 32 in the finite element program. Several components of the C_{ij} matrix are plotted as a function of radius at the maximum thickness section (Figure 16). Note that the coupling term between rz shear and axial strain is comparable in magnitude to the maximum shear stiffness. Note also the large increase in hoop stiffness between the inside and the outside of the billet. Under uniform temperature cooling, such unusual property distributions set up a predominantly tensile cross-ply normal stress field in the billet that reaches a maximum at about the mid-thickness of the billet. This condition, in conjunction with other processing stresses, significantly increases the risk of processing failure. The graphite phenolic ply properties as a function of temperature are shown in Table 3. Note that above 400° a chemical change is reflected in the thermal expansion coefficients.

4.1 CURING STRESS SENSITIVITY STUDY

Processing stresses during post-cure cool down were selected as the most likely thermomechanical condition contributing to delamination failure in the IUS billet. Subsequent data from the billet autopsy tend to confirm this selection. First, we establish the nature of the triaxial billet stress field during this processing step. Then, the sensitivity of these stresses to changes in the ply pattern orientation will be examined. Ply pattern orientation is a design parameter easily changed within the dimensional limits of the WCA graphite cloth, which is the raw material for the billet. Also, previous experience with laminates had indicated the potential for a sensitivity to ply orientation (Reference 9). Other important desig parameters, such as the basic shape of the pattern and mold die, are less easily changed and were not considered in this study.

36
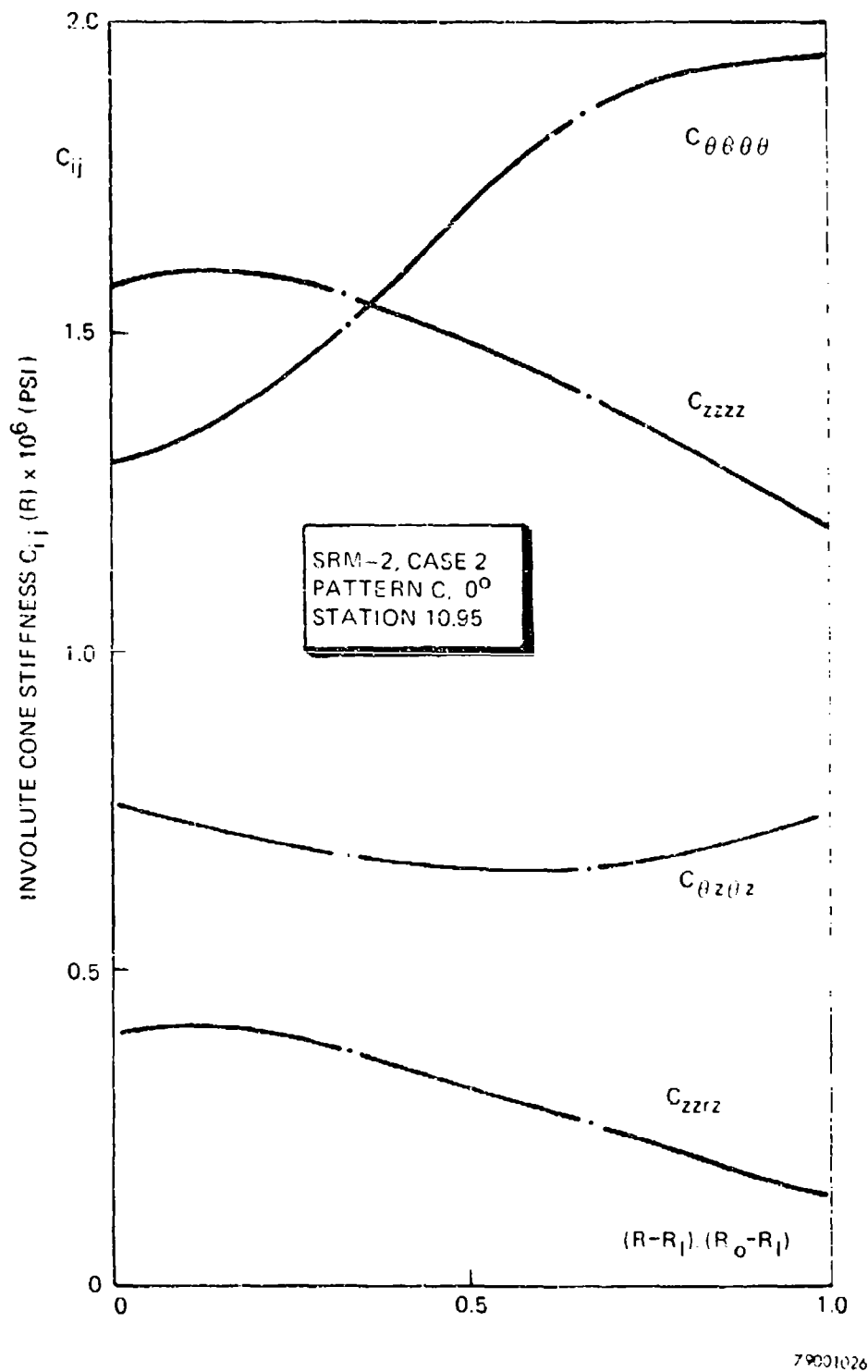
Figure 16. Stiffness Variations Through the Thickness

TABLE 3

GRAPHITE PHENOLIC NOMINAL POST-CURE PROPERTIES

T	E11	E22	E33
70°	1.90 msi (13.1 GP)	1.27 msi (8.8 GPa)	0.45 msi (3.1 GPa)
200°	1.60 msi (11.0 GP)	1.07 msi (7.4 GPa)	0.38 msi (2.6 GPa)
300°	1.33 msi (9.2 GP)	0.89 msi (6.1 GPa)	0.32 msi (2.2 GPa)
400°	1.10 msi (7.6 GP)	0.74 msi (5.1 GPa)	0.26 msi (1.8 GPa)
500°	0.87 msi (6.0 GP)	0.58 msi (4.0 GPa)	0.21 msi (1.4 GPa)
	G12	G13	G23
70°	0.80 msi (5.5 GP)	0.30 msi (2.1 GPa)	0.45 msi (3.1 GPa)
200°	0.67 msi (4.6 GP)	0.25 msi (1.7 GPa)	0.38 msi (2.6 GPa)
300°	0.56 msi (3.9 GP)	0.21 msi (1.4 GPa)	0.32 msi (2.2 GPa)
400°	0.46 msi (3.2 GP)	0.17 msi (1.2 GPa)	0.26 msi (1.8 GPa)
500°	0.37 msi (2.6 GP)	0.14 msi (1.0 GPa)	0.21 msi (1.4 GPa)
	$\alpha\ 11 \times 10^6$	$\alpha\ 22 \times 10^6$	$\alpha\ 33 \times 10^6$
70°	5.0/°F (2.7/°K)	7.0/°F (3.9/°K)	15.0/°F (8.3/°K)
200°	4.4/°F (2.4/°K)	8.1/°F (4.5/°K)	14.2/°F (7.9/°K)
300°	3.2/°F (1.8/°K)	6.9/°F (3.8/°K)	11.2/°F (6.2/°K)
400°	2.2/°F (1.2/°K)	4.6/°F (2.6/°K)	4.9/°F (2.7/°K)
500°	1.5/°F (.83/°K)	2.8/°F (1.6/°K)	-0.4/°F (-.22/°K)

The finite element analysis cases and the basic assumptions of this study are defined in Table 4. Another billet for the SRM-1 motor was analyzed at the same time, but these results, which are similar, are not included in this already lengthy report. Ply pattern C (Figure 17) was a minor change in pattern A made prior to the sensitivity study. The same mold die was used with both patterns, producing billets of the same dimension and very nearly identical stresses.

TABLE 4

SRM-2 PROCESS STRESS SENSITIVITY STUDY

Cases	Assumptions
1. Pattern A Orientation $\phi_0 = 0°$	1. Ideal Material (No defects)
2. Pattern C Orientation $\phi_0 = 0°$	2. Linear Elastic (Temperature-Dependent) Post-Cure Properties
3. Pattern C Orientation $\phi_0 = -90°$	3. Uniform Temperature Distribution in Billet
4. Pattern C Orientation $\phi_0 = -21°$	4. Billet Unconstrained (Free Boundary Conditions)
	5. Unit Temperature Change, $-100°F$ ($-56°K$)
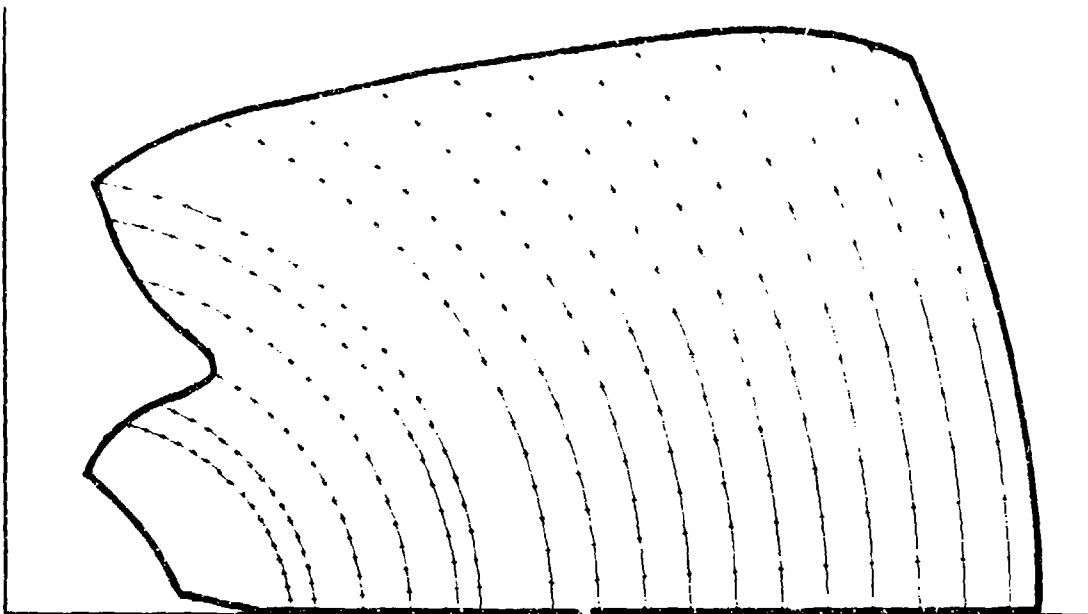
79001032

Figure 17.   Ply Pattern C Analysis Results

39

The structural response of the billet to uniform cooling is meridional bending that produces axial tension on the outside and axial compression on the inside over nearly the entire length of the billet (Figure 18). The associated hoop stresses are tension on the inside and compression on the outside, with the local maximums occurring at the inner and outer radii. These stress fields correlate well with the microcracking observed at 20X magnification during the autopsy. However, these stresses are not a serious threat to the billet, in that the material strength in these directions is many times the applied stress. Their significance lies in the interlaminar stress fields they induce, and it is these stresses which can lead to delamination at very low stress levels. These occur because of the very unusual stiffness properties described earlier (Figure 16) that cause the billet to bend and twist during cool down.

The interlaminar stress response will now be described using a series of contour stress plots for a single representative element. This allows their variation through the thickness to be shown in detail. Finite element number six was selected for examination (Figure 14) and it lies in a region that experienced massive delamination. Cracks extended from midthicknes .o the outer surface of the billet and followed closely the involute surface of a single ply. No initiation sites were found in the autopsy to indicate a local defect, and these delaminations extend over several inches in length. This is also a region in which the billet ply orientation data and the ply pattern analysis are in close agreement. The warp and the fill stress contours over element number six are shown in Figure 19 and, as stated earlier, they are small compared to the strength ^ a graphite phenolic ply. The cross-ply normal stress contours and the warp-fill shear stress contours are shown in Figure 20, and these require comment. First, note that the cross-ply normal stress is _tension_ with its maximum value, 10 psi per 100°F, occurring at midthickness. Also, note the relatively large warp-fill shear stress, 1 psi per 100°F, even compared with the warp and fill normal stresses. In flat laminates, cross-tension reduces transverse shear strength, not warp-fill (Reference 10); also, the

40
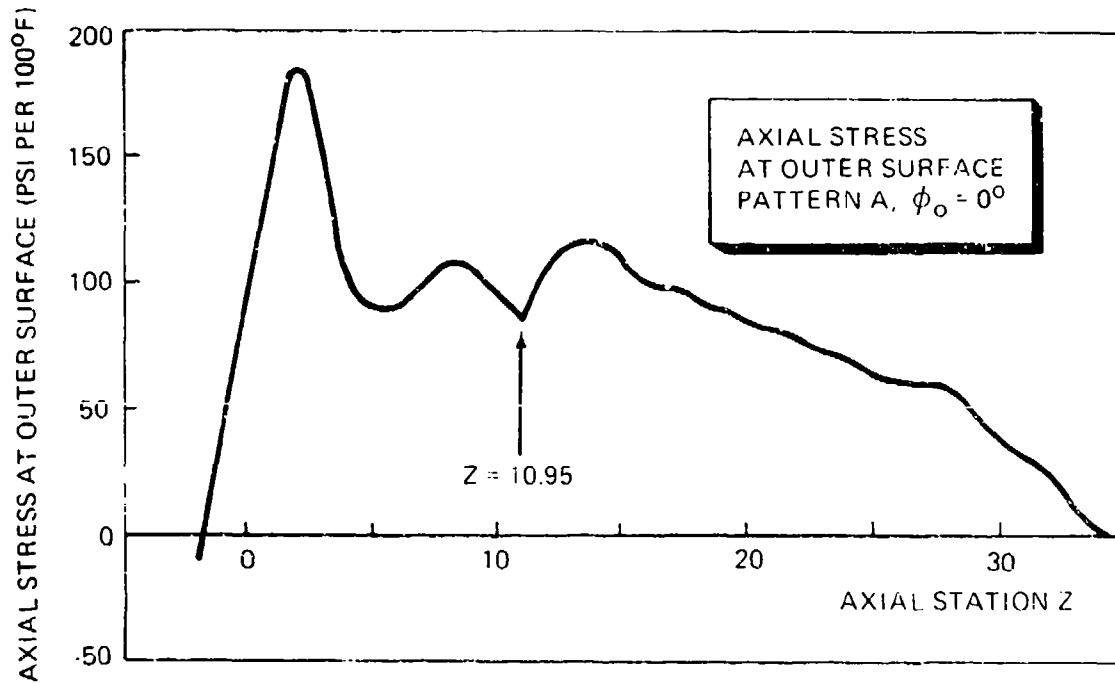
Figure 18. Axial Stress Distribution at Outer Surface
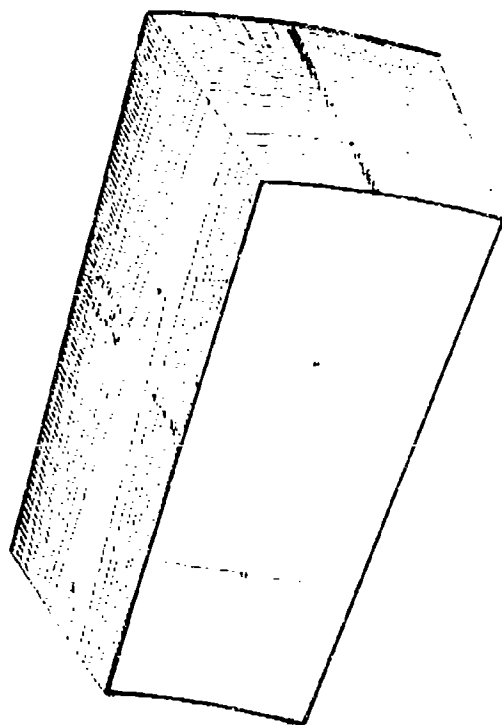
MAX = 20 PSI MIN = -280 PSI
WARP STRESS
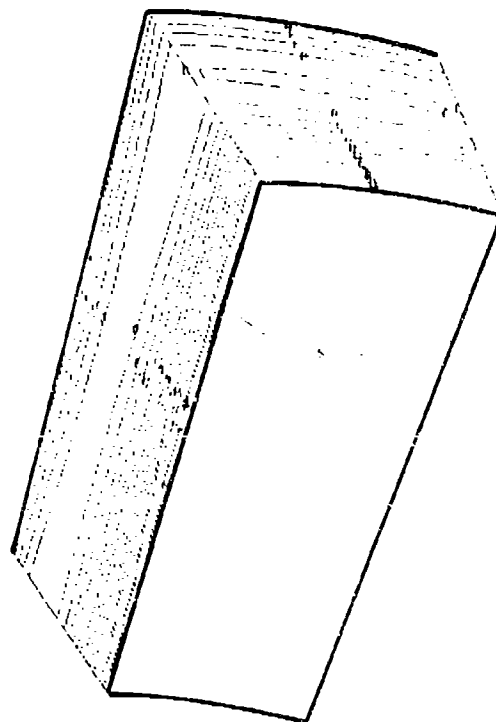
MAX = 210 PSI MIN = 20 PSI
FILL STRESS

79001017

Figure 19. Interlaminar Warp and Fill Stress Contours

MAX = 120 PSI MIN = -100 PSI   MAX = 10 PSI MIN = -1 PSI
WARP-FILL SHEAR STRESS   CROSS-PLY NORMAL STRESS
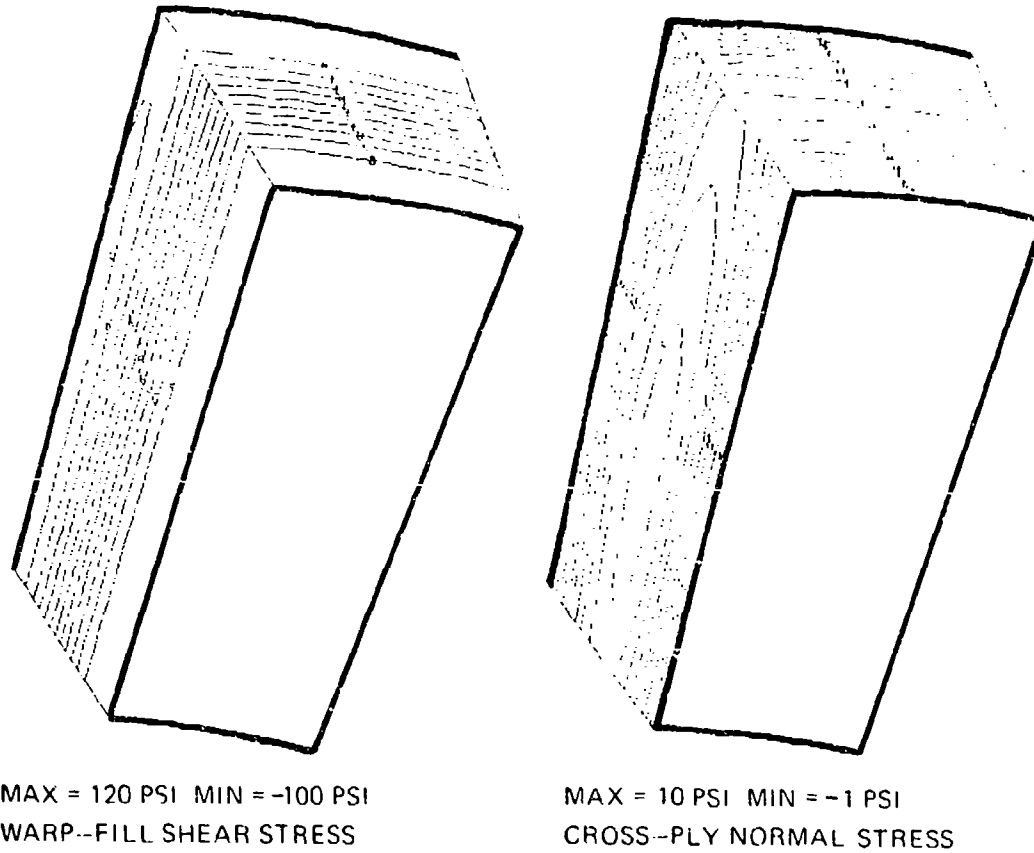
79001031

Figure 20. Interlaminar Normal and Warp-Fill Shear Stress Contours

43

sensitivity to defects or other anomalies increases sharply when cross-ply tension exists over a large volume of material. The cross-ply normal stress field shown for element number six is, in fact, typical of the first eight elements, with the maximum value, 34 psi per 100°F, occurring in element number three. Finally, the warp-normal and the fill-normal shear stresses are shown in Figure 21. They remain small every-where in the billet. These results characterize the interlaminar stress fields in the billet during cool down for both ply patterns A and C. The ability to focus, in depth, on interlaminar stress fields in critical areas is important to their understanding and to their control by the composite material designer.

Consider now what changes in the orientation of the pattern on the WCA graphite cloth can do to the critical interlaminar stresses. This was investigated for a 21° change and a 90° change in cases three and four, Table 4. To be comprehensive, a 180° range of orientations must be considered, but these two cases will show sensitivity. The 21° case represents the physical limit on orientation change caused by the width of the cloth. A comparison of cross-ply or normal stress (Figure 22) shows a dramatic change for the better, with the 90° case virtually eliminating this stress component. In fact, the magnitude is so low, that the model would have to be refined to obtain a precise thickness distribution. The change in warp-fill shear stress (Figure 23) is very nearly a mirror image in going from $\phi_0 = 0°$ to $\phi_0 = -90°$. It appears that individual interlaminar stress components may have different periods with respect to ϕ_0. They must all be periodic, of course, since a 180° rotation cannot be detected in the material stiffness distribution. It is also interesting to note that the $\phi_0 = -21°$ case has higher warp-fill shear stress than the other two cases. This orientation gives nearly uniform axial stiffness, but also produces a larger gradient in hoop stiffness. These stiffness changes produce changes in the structural response as well, and they are comparable to the interlaminar stress changes. The sense of the meridional bending moment, for example, is reversed for the $\phi_0 = -90°$ case. What these results indicate is that
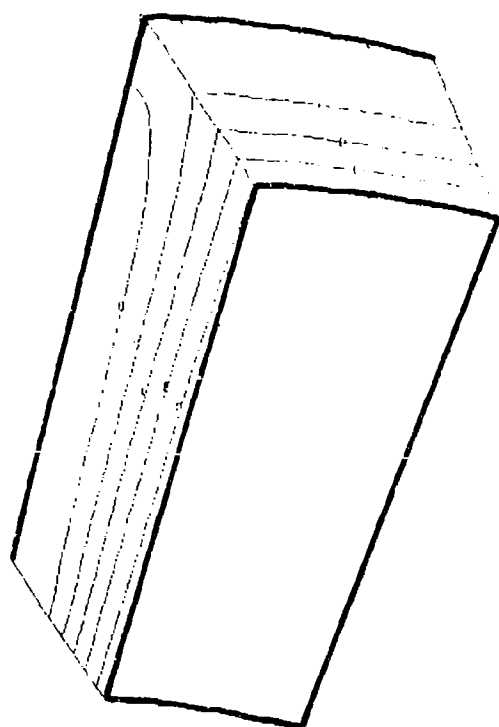
MAX = 15 PSI MIN = −15 PSI
FILL−NORMAL SHEAR STRESS
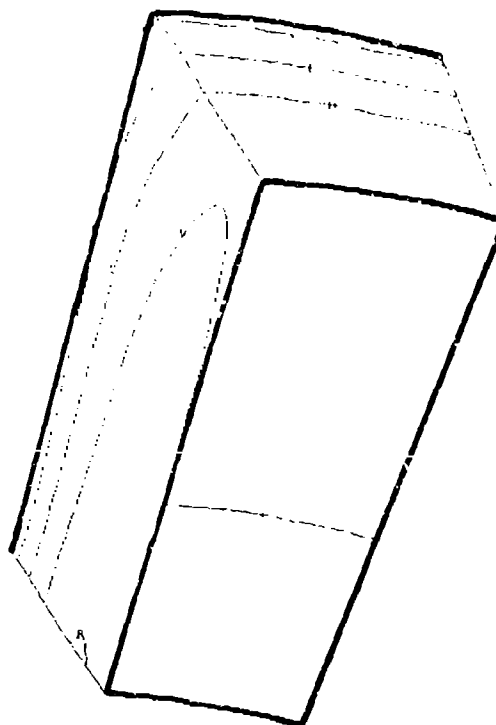
MAX = 15 PSI MIN = −15 PSI
WARP−NORMAL SHEAR STRESS

79001013

Figure 21.   Interlaminar Warp-Normal and Fill-Normal Shear Stress Contours
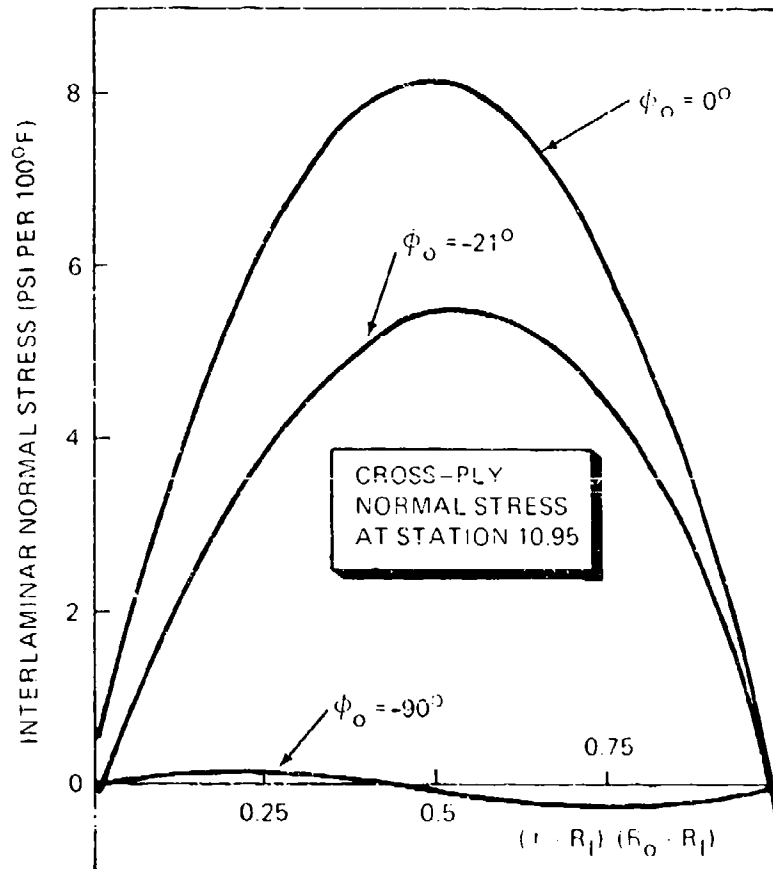
Figure 22. Orientation Sensitivity of Interlaminar Normal Stress
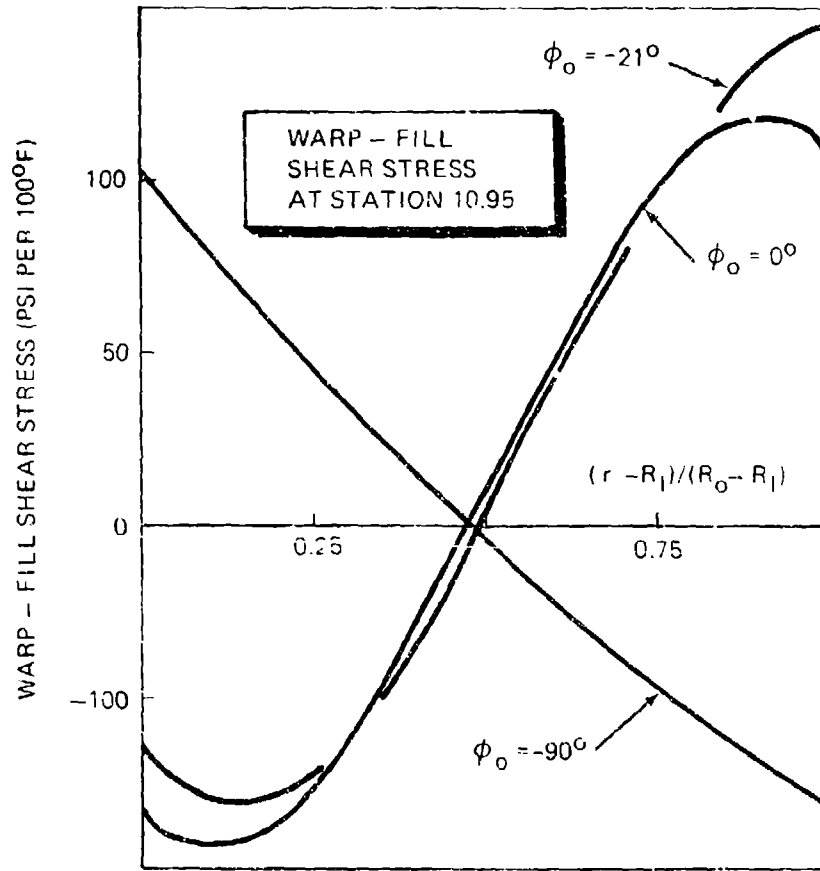
Figure 23.   Orientation Sensitivity of Warp-Fill Shear Stress

the processing stresses have a marked sensitivity to ply pattern orientation. Other design parameters, such as the number of plies, shape of the mold die, and cloth properties, are also likely to affect processing stresses.

SECTION V

CONCLUSIONS

An analysis procedure for determining the distribution of ply material in an involute body from the ply pattern has been developed and used in a study of processing stresses. The involute ply pattern analysis model produces Euler angle data that completely define the unusual stiffness properties of an involute body. They reduce the required material property data from 21 nonlinear functions of r and z to three quasi-linear functions, plus the ply material constants. Comparisons of the model with autopsy data show good agreement for warp orientation through the thickness of a billet and over most of the billet length. Only in the transition region where the cylindrical end intersects the main body of the exit cone, and ply distortions occur, are there significant differences.

A 3D finite element model with variable properties is defined for this class of materials based on the Euler angles output by the ply pattern analysis. This finite element is then applied to a processing stress study of an IUS exit cone billet that delaminated sometime during post cure. The bending and twisting response of the billet are shown to produce large areas of cross-ply tension during cooling. Stress fields predicted by the model were found to correlate well with the microcracking observed in the billet autopsy. A marked sensitivity of the interlaminar stress components to ply pattern orientation was then determined by analyzing orientations of 0°, 21°, and 90°. These results show the 90° orientation produces much lower processing normal stresses.

In summary, the present model should prove an effective tool for determining the complex stiffness distribution and the induced process stress fields within involute exit cones. It is clear that these stresses are sensitive to ply orientation and it is likely that they are sensitive to other design parameters not considered in the present study.

REFERENCES

1. Pagano, N. J., "Elastic Response of Rosette Cylinders Under Axisymmetric Loadings," AIAA Jour., Vol. 15, Feb. 1977, p. 159.

2. Wellman, B. L., Technical Descriptive Geometry, McGraw Hill Book Co., 1948.

3. Pagano, N. J., and Hsu, P. W., "Geometric Analysis of Rosette Exit Cones," Jour. Spacecraft and Rockets, Vol. 16, Sept-Oct 1979, p. 311.

4. Buch, J. D., and Pfeifer, W. H., "Process Stresses as Revealed by Microstructure and Microcracking." Presented at AFML Conference on Analysis and Fabrication of Carbon-Carbon Involute Exit Cones, Dayton, Ohio, 1979.

5. Crose, J. G., "Structural Mechanics of Involute Exit Cones." Presented at 1979 JANNAF Propulsion Meeting, Anaheim, Calif., March 1979.

6. Stanton, E. L., "A General Three-Dimensional Computational Model for Nonlinear Composite Structures and Materials." AIAA Paper No. 77-360, Proceedings AIAA/ASME 18th SDM Conference, 1977, pp. 9-22.

7. Stanton, E. L., Crain, L. M., and Neu, T. F., "A Parametric Cubic Modelling System for General Solids of Composite Material," Int. J. Num. Methods Engng., Vol. 11, 1977, pp. 653-570.

8. Davis, H. O., "Behavior of Involute Structures, Predicted and Measured." AIAA Paper No. 79-1216, Presented at AIAA/SAE/ASME 15th Joint Propulsion Conference, Las Vegas, June 1979.

9. Pagano, N. J., and Pipes, R. B., "The Influence of Stacking Sequence on Laminate Strength," Jour. Composite Materials, Vol. 5, Jan. 1971, pp. 50-57.

10. Hahn, H. T., and Erikson, J., "Representation of Matrix/Interface Controlled Strength of Unidirectional Composites," AFML-TR-78-85, Aug. 1978.